

# 1 Borehole-based characterization of deep crevasses at a Greenlandic 2 outlet glacier

3 **Bryn Hubbard<sup>1</sup>, Poul Christoffersen<sup>2</sup>, Samuel H. Doyle<sup>1</sup>, Thomas R. Chudley<sup>2</sup>, Charlotte M. Schoonman<sup>2</sup>,**  
4 **Robert Law<sup>2</sup>, Marion Bougamont<sup>2</sup>**

5 <sup>1</sup>Centre for Glaciology, Department of Geography and Earth Sciences, Aberystwyth University, Aberystwyth,  
6 UK. <sup>2</sup>Scott Polar Research Institute, University of Cambridge, Cambridge, UK.

7 **Correspondence to:** Bryn Hubbard (byh@aber.ac.uk)

## 8 **Key Points:**

- 9 • Borehole logging by optical televiewer reveals the presence of numerous deep, high-angle crevasse  
10 traces at Store Glacier, Greenland.
- 11 • Crevasse traces are observed to a depth of 265 m and crevasses are inferred to a depth of 400 m.
- 12 • Crevasse traces present planes of weakness and show evidence of multiple reactivation phases, in  
13 some cases annual, during passage through the glacier.

14 **Abstract** Despite the inferred importance of deep surface crevasses to ice-mass deformation, mass  
15 redistribution and latent energy transfer, no observations of such crevasses have yet been reported. Optical  
16 televiewer (OPTV) logging of a 325 m-deep borehole drilled within a crevassed region of fast-moving Store  
17 Glacier, Greenland, revealed the presence of 35 high-angle crevasse traces that cut across the background  
18 primary stratification. Twenty-eight of these traces were formed of a bubble-free layer of refrozen ice that  
19 hosted one or more mm-thick laminae of bubble-rich 'last frozen' ice. Several such last-frozen laminae were  
20 observed in four traces, indicating multiple episodes of crevasse reactivation. In one notable case, nine such  
21 laminae were observed, indicating four, likely annual, reactivation events. Inspection of the full OPTV log  
22 reveals the frequency of crevasse traces generally decreased with depth, and that the deepest detectable  
23 trace was 265 m below the surface. This is consistent with the extent of the warmer-than-modelled englacial  
24 ice layer in the area, which extends to ~400 m below the surface. We conclude that deep crevassing is  
25 pervasive across Store Glacier, and therefore also at dynamically similar Greenlandic (and likely Antarctic)  
26 outlet glaciers. Once healed, the traces of these crevasses represent planes of weakness that may be  
27 reactivated during their subsequent passage through the glacier. Given their depth and continuing formation,  
28 it is highly likely that such traces survive ablation to reach the glacier terminus, presenting foci for rifting and  
29 iceberg calving.

30 **Plain language summary** Crevasses in the surface of ice masses allow ice-mass motion and the transfer of  
31 water and the heat it holds into the ice mass' interior. Crevasses extending deeper than some tens of metres  
32 have been inferred from indirect evidence such as radar scattering but have not been observed directly. Here,  
33 we evaluate the presence and properties of such deep crevasses by using an optical televiewer (OPTV) to  
34 record a continuous high-resolution image of the complete wall of a borehole drilled to a depth of 325 m in  
35 Store Glacier, a heavily-crevassed fast-moving outlet glacier of the Greenland Ice Sheet. The OPTV image  
36 intersects multiple now-closed crevasses to a depth of 265 m, many of which show evidence of multiple  
37 phases of opening and closing as they have been carried through the glacier to the location of our borehole.  
38 We infer that, at least in fast-moving glaciers such as Store, deep crevasses are pervasive, may be regenerated  
39 several times, and are able to transfer water and heat from the surface to depths of at least 400 m. The  
40 crevasses we image are sufficiently deep to survive surface melting to the glacier terminus, where they act  
41 as planes of weakness, enabling ice fracture and iceberg calving.

## 42 **1 Introduction**

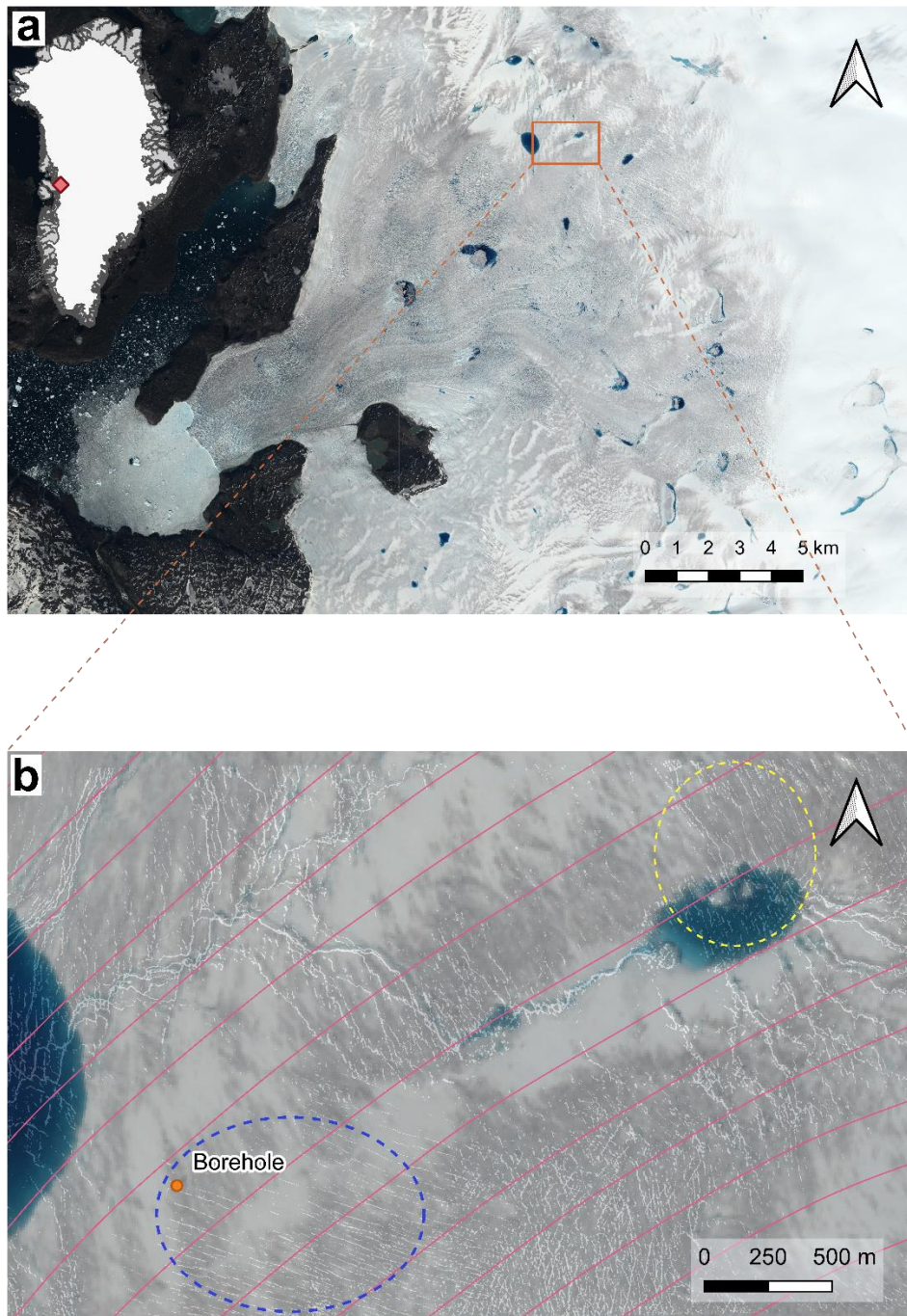
43 Surface crevasses facilitate bulk ice motion and serve as pathways to transfer water and its thermal energy  
44 from the surface of an ice mass to its subsurface. Theoretically, creep closure limits the depth of dry crevasses  
45 to some tens of metres (see Mottram & Benn, 2009; Nye, 1955), but this can be increased substantially by  
46 hydrofracturing of water-filled crevasses (van der Veen, 1998; Weertman, 1973). Once initiated,  
47 hydrofracture extends the tip and, if enough water is available to increase its depth accordingly, propagation  
48 can continue to the glacier bed. This mechanism has been used to explain the rapid transfer of meltwater to  
49 the glacier bed during discrete surface lake drainage events (e.g., Chudley, Christoffersen, Doyle, Bougamont,  
50 et al., 2019; Das et al., 2008; Doyle et al., 2013), common through ice up to ~1 km thick around the margins  
51 of the Greenland Ice Sheet (GrIS) and at a smaller scale on, for example, Ellesmere Island, Canada (Boon &  
52 Sharp, 2003).

53 In the absence of lake-drainage driving crevasses to the glacier bed, at least three general lines of  
54 evidence suggest the presence of deep, englacially-terminating crevasses. First, such crevasses have been  
55 considered responsible for englacial warming as a result of energy released by meltwater refreezing within  
56 them (e.g., Colgan et al., 2011; Poinar et al., 2017), so-called ‘cryo-hydrologic warming’ (Phillips, Rajaram, &  
57 Steffen, 2010). For example, Lüthi et al. (2015) favoured refreezing of meltwater in 300 – 400 m deep  
58 crevasses to explain englacial ice temperatures measured in boreholes near the western margin of the  
59 Greenland Ice Sheet. These ice temperatures were recorded to be 10 – 15 °C warmer than modelled by heat  
60 diffusion alone. More recently, Seguinot et al. (2020) invoked the same process to explain measured englacial  
61 warming at a rate of 0.39 °C a<sup>-1</sup> in englacial ice advancing towards the terminus of tidewater Bowdoin Glacier,  
62 Greenland. Here, it was considered that the crevasses, which possibly initiated in association with band  
63 ogives several km upglacier, may have warmed the glacier’s full thickness of ~250 – 300 m. Such inferences  
64 are not limited to the margins of the GrIS. For example, Gilbert et al. (2020) suggested that meltwater  
65 refreezing in crevasses may be responsible for deep warming, inferred from surface ground-penetrating  
66 radar, at Rikha Samba Glacier, Nepal, a process that may also contribute to anomalously warm englacial ice  
67 measured in boreholes across the debris-covered tongue of Khumbu Glacier, Nepal (Miles et al., 2018).  
68 Second, deep englacially terminating crevasses have also been invoked to explain englacial radar scattering.  
69 For example, Catania et al. (2008) interpreted single englacial diffractors from 1 MHz surface radar transects  
70 in Greenland as reflections from the apex of deep crevasses, in this case from depths of ~100 – 200 m (their  
71 Figure 2). Third, inferred crevasse traces have been observed in ice near the glacier bed during exploration  
72 of ice-marginal subglacial cavities and tunnels (e.g., Hubbard, Cook, & Coulson, 2009; Lovell et al., 2015),  
73 implying initial propagation to depths of greater than some tens of metres. Hambrey (1976) calculated this  
74 depth (from cumulative overburden mass loss) to be at least 80 m from observations of surface crevasse  
75 traces in the ablation area of Charles Rabots Bre, Norway. However, in these cases there is some uncertainty  
76 involved in determining confidently whether such features were originally deep surface crevasses or local  
77 basal crevasses.

78 Strong inferential evidence therefore exists for the occurrence of crevasses extending >10s m below the  
79 ice surface. However, gaining direct access to such crevasses is effectively impossible and no first-hand  
80 observations of their presence or depth have yet been reported. One means of acquiring such evidence lies  
81 in imaging the wall of a borehole drilled to intersect crevasse traces that have deformed such that they are  
82 no longer vertical. In this paper we report on the application of borehole optical televiewer (OPTV) logging  
83 to ascertain the presence and properties of deep crevasses within Store Glacier, a fast-moving outlet glacier  
84 of the GrIS.

## 85 2 Field site and methods

86 Store Glacier (Greenlandic name *Sermeq Kujalleq*) is a fast-moving ice stream draining the central-west sector  
87 of the GrIS into Davis Strait via Ikerasak Fjord in the Uummannaq Fiord system (Figure 1).



88

89 **Figure 1.** (a) Basemap image of Store Glacier, Greenland, and (b) expansion of (a) showing superimposed crevasse  
 90 patterns from a UAV-generated digital elevation model (Chudley, Christoffersen, Doyle, Abellan, & Snooke, 2019). The  
 91 smooth red lines indicate ice surface flow lines (NE to SW) derived from the MEaSURES velocity dataset (Joughin, Smith,  
 92 Howat, Scambos, & Moon, 2010), and the areas enclosed by the dashed lines identify dominant (planform) crevasse  
 93 orientations of  $290^{\circ}/110^{\circ}$  around the borehole (blue) and of  $350^{\circ}/170^{\circ}$   $\sim 3 - 4$  km upflow of the borehole (yellow).

94 The borehole investigated herein (BH18c) is located within a crevassed area  $\sim 30$  km from the terminus of  
 95 Store Glacier and within some km of a supraglacial lake that drains rapidly via hydrofracture during most  
 96 summers (Chudley, Christoffersen, Doyle, Bougamont, et al., 2019). Although the area is generally crevassed,  
 97 BH18c was drilled  $\sim 5$  m away from the nearest open crevasse, both for reasons of operator safety and to  
 98 minimise the chances of the vertical borehole intersecting the (assumed vertical) crevasse. Locally, ice surface  
 99 velocity is  $\sim 700$  m  $a^{-1}$ , achieved largely through basal motion focussed at a temperate interface (Doyle et al.,  
 100 2018) between ice and an underlying deformable subglacial sediment layer (Hofstede et al., 2018). Although  
 101 drilling (by hot pressurized water) was halted temporarily to allow logging, the borehole was eventually  
 102 drilled to the bed at a depth of  $\sim 949$  m. The uppermost 325 m of this borehole was logged by optical

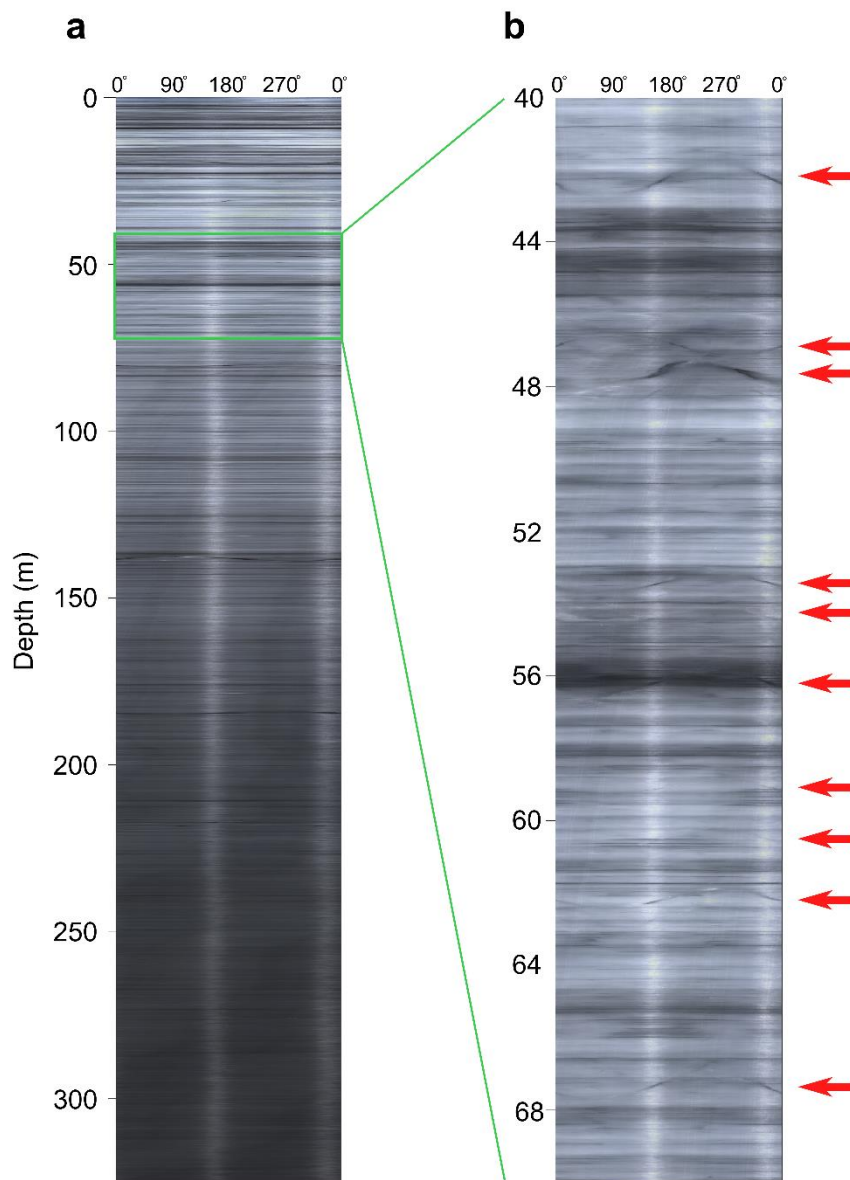
103 televiewer (OPTV), providing a geometrically accurate RGB image of the complete borehole wall at a  
104 resolution of  $\sim 1$  mm both vertically and laterally. Such OPTV images have the capacity to inform on annual  
105 accumulation (Philippe et al., 2016), the presence and scale of refrozen layers within firn (Hubbard et al.,  
106 2016), marine ice accretion (Hubbard et al., 2012) and visible structural features intersecting the borehole  
107 wall (Roberson & Hubbard, 2010). For example, the last of these studies identified eight separate ice  
108 structures, including high-angle crevasse traces to a depth of some tens of metres, in the ablation area of  
109 Midtre Lovénbreen, Svalbard. Since OPTV images extend around the entire (cylindrical) borehole wall, they  
110 are typically unrolled for 2D presentation, extending left to right around the compass (N-E-S-W-N or  $0^\circ$ - $90^\circ$ -  
111  $180^\circ$ - $270^\circ$ - $0^\circ$ ). Planar layers appear as sinusoids on such 2D images, with the amplitude of the sinusoid  
112 representing the layer's dip and the phase of the sinusoid its azimuth or strike (Hubbard, Roberson, Samyn,  
113 & Merton-Lyn, 2008). Structural analysis and plotting were carried out using software packages BiFAT  
114 (Malone, Hubbard, Merton-Lyn, Worthington, & Zwiggelaar, 2013), WellCAD, and Stereonet v.11 (Cardozo &  
115 Allmendinger, 2013).

116 Borehole temperatures were recorded by sensor strings installed into two boreholes, BH 18b and  
117 BH18d, both located  $<10$  m from BH18c. Englacial temperature was measured using thermistors (see Doyle  
118 et al., 2018) and DS18B20 digital temperature sensors (Table S1; Figure S1). Undisturbed ice temperatures  
119 were estimated following established methods (Doyle et al., 2018; Humphrey & Echelmeyer, 1990). A  
120 theoretical borehole temperature profile was also created by inverting the 2016 annually observed  
121 MEASUREs surface ice velocity using the higher-order Community Ice Sheet Model 2.0, which conserves  
122 momentum, mass and thermal energy in three dimensions. The approach follows that used by Price et al.  
123 (2011) for Greenland and Bougamont et al. (2019) for Antarctica. The observed motion was simulated by first  
124 prescribing a no-slip basal boundary condition, and then subtracting the derived internal ice deformation  
125 from the observed surface velocities. We then iterated basal traction and sliding rates to an equilibrium in  
126 which ice temperature, effective ice viscosity, and ice velocity fields converged with the target velocities. To  
127 constrain the inversions, we used BedMachine v.3 ice thickness and bed topography (Morlighem et al., 2017)  
128 resampled to the 1 km fixed grid of our model. Surface air temperature was specified at the same 1 km  
129 resolution using output from the RACMO regional climate model (Noël et al., 2018).

## 130 3 Results

### 131 3.1 OPTV log

132 The complete 325 m long OPTV log of BH18c (Figure 2a) shows two general characteristics.



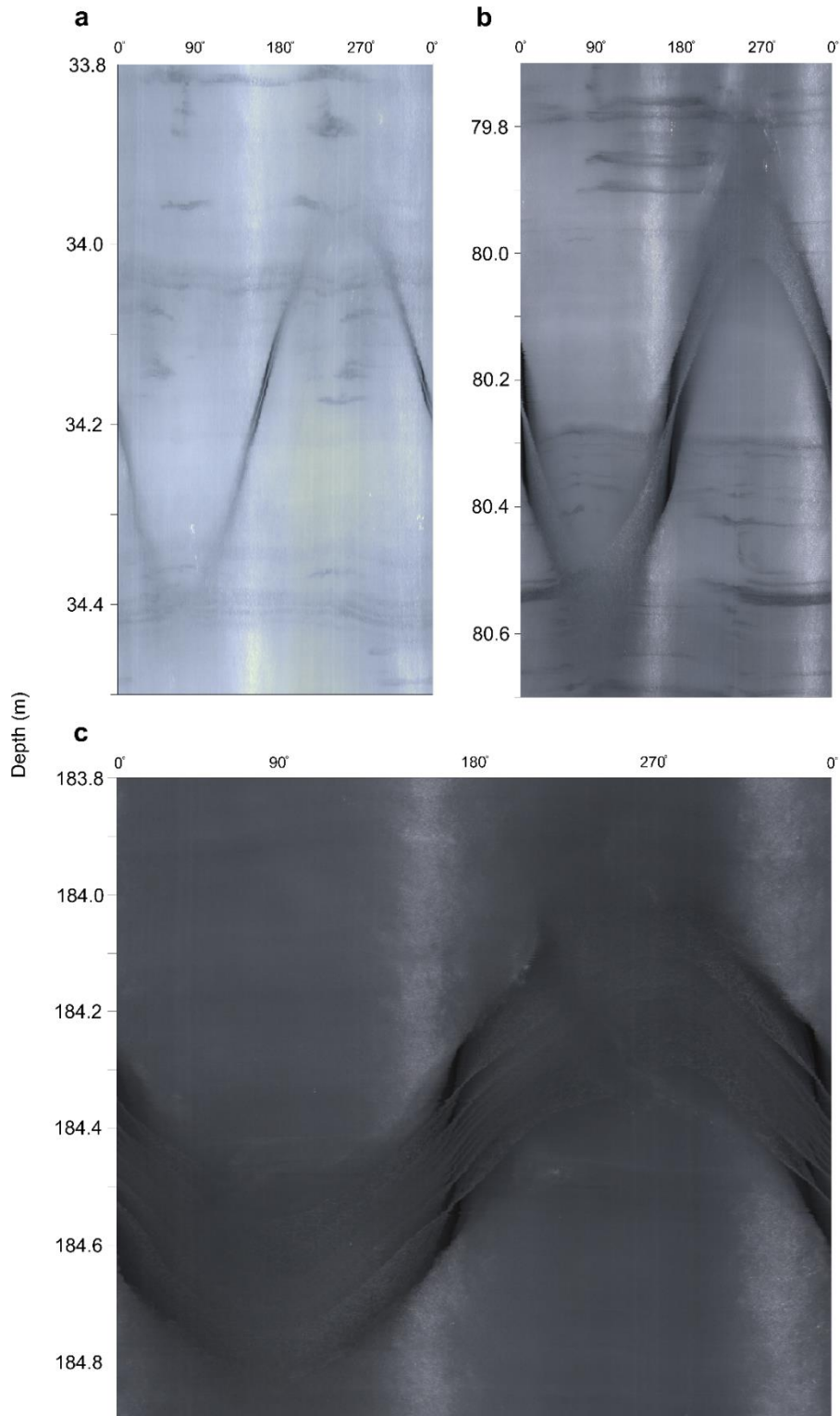
133

134 **Figure 2.** OPTV log of BH18c. (a) The complete 325 m-long log (note  $\sim 150$  x vertical compression), and (b) expansion  
 135 ( $\sim 15$  x vertical compression) of depth range 40 - 70 m showing 10 high angle sinusoids (planes in 3D space), each marked  
 136 by a red arrow, cutting across low-angle background layers. With a borehole diameter of  $\sim 12$  cm, the width of these  
 137 OPTV images is the borehole circumference,  $\sim 0.38$  m. Note, the reflective (brighter) sub-vertical streaks at  $\sim 160^\circ$  and  
 138  $\sim 340^\circ$  are drilling artefacts, probably caused by contact between the hose and borehole wall.

139 First, the log shows an overall decrease in luminosity with depth. This is common to many OPTV logs  
 140 recovered from glacier boreholes (Hubbard et al., 2013), with light scattering decreasing with depth as the  
 141 material forming the borehole wall progresses from highly reflective snow and firn through bubble-rich ice  
 142 of intermediate reflectivity to almost transparent bubble-poor ice at depth. Since BH18c is in the ablation  
 143 area of Store Glacier, it intersects no near-surface snow or firn, and the darkening in this case represents a  
 144 general decrease in bubble content with depth. Second, numerous alternating decimetre-scale light and dark  
 145 bands signify alternating bubble-rich 'white' ice and bubble-poor transparent ice (Figure 2b). This banding  
 146 extends throughout the full depth of the OPTV log and, although appearing uniform and horizontal at the  
 147 (vertically compressed) scale illustrated in Figure 2a, an expanded section (Figure 2b) reveals that the banding  
 148 dips shallowly and is of highly variable thickness around the borehole.

149 Closer inspection of the OPTV log of BH18c also reveals the presence of 35 distinct high-angle layers  
 150 (examples of which are indicated by red arrows in Figure 2b) that cut across the less distinct, lower-angle  
 151 banding noted above. Enlargements of the log (Figure 3) reveal that these layers form regular sinusoids,

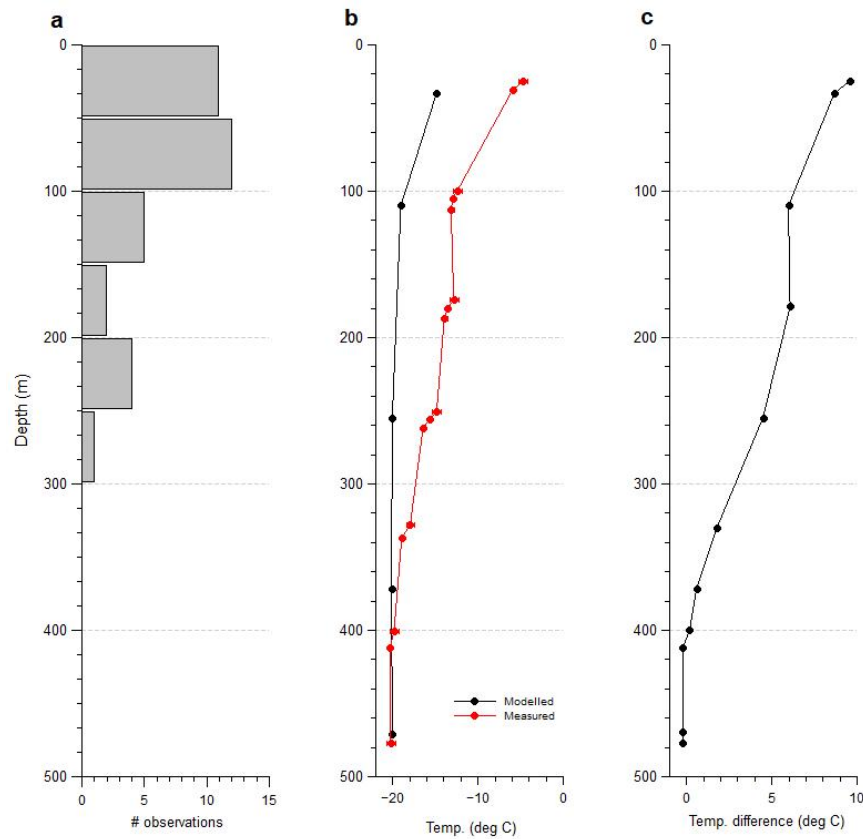
152 indicating correspondingly uniform and planar layers in 3D space. Each layer is formed of one or more thin  
153 (~mm scale) laminae that is bright (reflective) and hence bubble-rich. In 28 cases these laminae are enveloped  
154 by cm- to tens of cm-thick layers of ice that appear dark and are hence transparent and devoid of reflective  
155 bubbles. Of these 28 layers, 24 host a single central lamina (e.g., Figure 3a and b), one hosts two such laminae,  
156 two host three such laminae, and one (a ~0.25 m-thick layer at a depth of ~184 m) hosts nine such laminae  
157 (Figure 3c).



158  
159 **Figure 3.** Selected expanded sections of the OPTV image of BH18c (shown in Figure 2), illustrating high-angle planar  
160 layers, apparent as a sinusoid in these 2D representations: (a) 33.8 – 34.5 m depth, (b) 79.7 – 80.7 m depth, and (c)

161 183.8 – 184.9 m depth. Note the general decrease in luminosity with depth and the central bubble-rich (bright) planar  
162 layers bisecting the high-angle layers imaged in (a) and (b) and the presence of multiple such layers in (c).

163 Analysis of the depth distribution of the 35 high-angle layers intersected by BH18c (Figure 4a) shows  
164 a general decline in frequency with depth, with the deepest observed plane being 265 m below the glacier  
165 surface. It is quite possible that the borehole intersected similar planes below this depth but that they were  
166 indistinguishable from the background ice. This is because (visibly bright) included bubbles are progressively  
167 expelled from all ice as pressure increases at depth, homogenizing the darkening OPTV image.

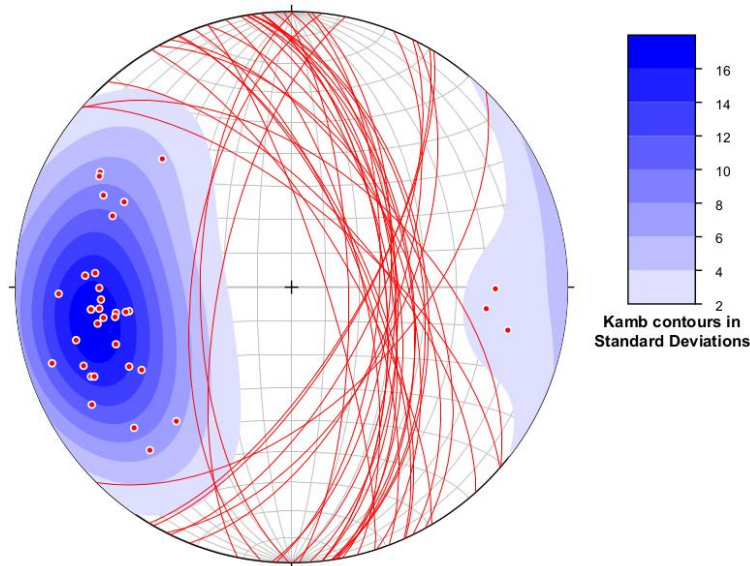


168

169 **Figure 4.** Key properties of the uppermost 325 m of BH18c at Store Glacier: (a) histogram of the number of high-angle  
170 planes identified in the OPTV log, (b) modelled (black dots) and measured (red dots) englacial temperatures for the  
171 overlapping sections of the two records, and (c) difference ('residual temperature') between the measured and  
172 modelled temperatures presented in (b).

173 Geometrical analysis of the orientation of these planes reveals a strong single maximum dipping approximately west to  
174 east (mean azimuth of pole to plane = 262°) at a mean dip of 63° (Figure 5 and Table 1).

175



176

177 **Figure 5.** Lower hemisphere equal-area plot of all high-angle planes identified in the OPTV log of the uppermost 325 m  
 178 of BH18c. Planes are plotted as red lines and poles to those planes as red dots, contoured by standard deviation  
 179 following Kamb (1959). Eigen analysis data are given in Table 1.

180 Accordingly, eigen analysis of the poles to these planes (plotted as red dots on Figure 5) indicates a dominant  
 181 principal eigenvalue of 0.83 at a principal vector of 262°/63° (Table 1).

182 **Table 1.** Eigen analysis data summarizing the 3D orientation of all 35 high-angle poles to planes, plotted as dots on  
 183 Figure 5, identified in the OPTV log of the uppermost 325 m of BH18c.

Axis	Eigenvalue	Eigenvector	
		Azimuth (°)	Dip (°)
1	0.83	262	63
2	0.10	165	75
3	0.07	50	31

184

### 185 3.2 Englacial ice temperature

186 The borehole sensor strings recorded 32 discrete ice temperatures between the near-surface and the ice-  
 187 bed interface (Figure S1). These temperatures decrease from ~-5 °C at a depth of ~25 m (the uppermost  
 188 thermistor location in the borehole) to ~-22 °C at 600 – 700 m depth, to rise again sharply to temperate at  
 189 the bed at a depth of ~949 m. Over most of the borehole length, the modelled temperatures correspond  
 190 closely with the measured temperatures (Figure S1). However, modelled temperatures diverge from the  
 191 observed record in the depth ranges 0 – ~400 m and 770 - 850 m. The former of these is relevant to the  
 192 present study, and temperature data over the depth range 0 – 500 m are plotted in Figure 4b. Measured  
 193 temperatures are notably higher than modelled temperatures, a difference ('residual temperature') that  
 194 decreases with depth from ~10 °C near the surface to zero at ~400 m (Figure 4c).

## 195 4 Interpretation and discussion

196 The background (host) ice is formed of alternating sub-horizontal, but irregular, bands of bright bubble-rich  
 197 ice and darker bubble-poor ice at the scale of cm to tens of cm. This is typical of the remnants of primary  
 198 stratification in englacial ice, with the bands having originally been laid down as snowfall in the accumulation  
 199 area of the GrIS. Such primary stratification has been identified elsewhere, both at the glacier surface (see

200 review by Hambrey & Lawson, 2000) and within borehole OPTV logs (Roberson & Hubbard, 2010).  
201 Superimposed onto this primary structure, the high-angle planes have the physical properties of healed  
202 crevasses or crevasse traces. These properties include their secondary status (cutting across the primary  
203 stratification), high angle, and planar geometry. The clear nature of the transparent ice forming these layers  
204 is consistent with formation by the refreezing of a water-filled crack some cm to tens of cm across. Such ice  
205 is typical of refrozen ice from which gas has been expelled during the freezing process (e.g., Pohjola, 1994),  
206 as are their bubble-rich central laminae. Here, gas is rejected at the advancing ice front, increasing its  
207 concentration in the remaining reservoir of unfrozen water, eventually reaching saturation. At that point,  
208 bubbles form and are incorporated as a lamina into the last-frozen ice layer (Hubbard, 1991). The central  
209 position of the bubble-rich last-frozen lamina we observe in most of the OPTV image of BH18c (Figures 3a  
210 and b) is consistent with water freezing inwards at a similar rate from both edges a crevasse. Similar features,  
211 also interpreted as crevasse traces, have been identified cropping out at the glacier surface (e.g., Figure 6).  
212



213

214 **Figure 6.** Photograph of a surface exposure of a set of sub-vertical crevasse traces at Trapridge Glacier, Canada (Hambrey  
215 & Clarke, 2019; their Figure 7d). Note the planar crevasse traces cut across the host ice and are generally clear with a  
216 bubble-rich central plane, like those in our OPTV images shown in Figure 3.

217 Where exposed at the glacier surface, such clear ice crevasse traces commonly erode preferentially, providing  
218 ready channels for supraglacial drainage (Hambrey & Müller, 1978) (also see Figure S2). We interpret multiple  
219 last-frozen laminae within a crevasse trace, such as that imaged at a depth of 184 m (Figure 3c), in terms of  
220 the effects of multiple separate refreezing events. Although multiple central laminae have not, to our  
221 knowledge, been reported elsewhere, reactivation of crevasse traces as thrust faults has been proposed (e.g.,  
222 Goodsell, Hambrey, Glasser, Nienow, & Mair, 2005). Since the crevasse traces we image at Store Glacier  
223 overprint, but do not displace, the primary stratification (Figure 3), the crevasses appear to have formed by  
224 Mode I ‘opening’ with little or no accompanying shearing (Mode II ‘sliding’ or Mode III ‘tearing’). Accordingly,  
225 we envisage reactivation of an existing crevasse trace to involve opening along its bubble-rich last-frozen  
226 lamina and splitting that layer into two thinner bubble-rich laminae. The open crevasse then refills with  
227 meltwater that eventually refreezes itself, forming a new (third) bubble-rich last-frozen lamina. After that,  
228 any subsequent reactivation can open any of the three pre-existing last-frozen laminae and the process is  
229 repeated, each time adding a pair of new laminae and therefore generally resulting in an odd total number  
230 of such laminae. This is consistent with our observations, and in particular with the feature at 184 m depth  
231 which has nine such laminae (Figure 3c), indicating the initial crevasse trace was reactivated four times. In  
232 contrast, we imaged one high-angle layer with an even number of central laminae (two). In this case, the  
233 crevasse could have reactivated along a new plane rather than along the pre-existing central laminae. If this  
234 were the case then, of the 28 filled crevasse traces imaged in the uppermost 325 m of BH18c, 24 showed no  
235 clear evidence of reactivation, three showed evidence of a single reactivation phase, and one showed  
236 evidence of four reactivation phases. Of these seven inferred reactivation phases, six occurred along a pre-  
237 existing bubble-rich last-frozen lamina. The seven bright laminae that were not visually bounded by

238 transparent (refrozen) ice likely formed as dry crevasses, the traces of which consequently did not host a  
239 refrozen ice layer.

240 Geometrical analysis of the crevasse traces intersected in BH18c (Figure 5) indicates a strongly  
241 clustered distribution centered on a dip of  $63^\circ$  in an approximately west-to-east direction. The poles to these  
242 planes are clustered at an azimuth of  $262^\circ$ , indicating that the strike of the plane is  $352/172^\circ$ . Reference to  
243 Figure 1b shows that this orientation is inconsistent with that of crevasses cropping out at the glacier surface  
244 locally (bounded by the dashed blue line in Figure 1b), which trend  $\sim 290/110^\circ$ , but is almost identical to that  
245 of a crevasse field located  $\sim 3 - 4$  km upflow of BH18c (bounded by the dashed yellow line in Figure 1b), which  
246 trends  $\sim 350/170^\circ$ . All 35 crevasse traces imaged in BH18c therefore appear to have been formed some  
247 kilometres upflow and to have advected to the borehole. Indeed, it is this flow that has allowed them to  
248 deform sufficiently away from vertical to be intersected by the (vertical) borehole. This also explains why  
249 BH18c appears to have intersected no local crevasses (trending  $270/90^\circ$ ), since these are presumably still  
250 undeformed and therefore close to vertical, reflecting their Mode 1 nature, while the borehole was drilled  
251  $\sim 5$  m equidistant from the nearest crevasses. Since local crevasse spacing is typically  $\sim 5 - 10$  m (Figure S2),  
252 this absence of intersection indicates that these crevasses are shallow and/or do not deviate significantly  
253 from vertical over their entire depth range. Further, with a local surface ice velocity of  $\sim 700$  m  $a^{-1}$ , it would  
254 take these newly formed crevasses  $\sim 5$  a to advect to the borehole. The crevasse trace intersected at a depth  
255 of 184 m (Figure 3c), which shows four reactivation phases, could therefore have been reactivated annually.  
256 In this case the crevasse would be expected to open, providing a meltwater reservoir and possible drainage  
257 pathway, in the late spring or summer, when the ice speeds up and meltwater becomes available, and  
258 refreeze when that opening and filling are no longer able to resist inwards refreezing from the cold crevasse  
259 walls.

260 It takes  $\sim 40$  years for ice to move from the location of our borehole to the front of Store Glacier,  
261 during which time  $\sim 100$  m of surface ice would be lost to ablation (assuming a surface ablation rate of  $2.5$  m  
262  $a^{-1}$ ). Thus, crevasse traces deeper than this at the borehole site, as well as those formed deep enough farther  
263 down-glacier, would survive to the glacier's terminus, some to depths of 100s of m. Where this is the case,  
264 such traces will almost certainly continue to present sub-vertical planes of weakness, offering locations of  
265 preferential brittle failure for rifting and iceberg calving.

266 The frequency of intersected crevasses with depth is irregular but shows a general decrease (Figure  
267 4a). Assuming this depth distribution represents that of the original crevasses, then only seven (or 20%) of  
268 the 35 intersected by the borehole were shallower than 40 m depth and 12 (34%) were deeper than 100 m.  
269 Although specific to our study site, the relationship between the crevasses present (%) per 30 m depth range  
270 ( $C(30)\%$ ) and depth ( $D$ , m), as illustrated in Figure 4a, can be approximated ( $R = 0.69$ ) as a logarithmic function:

$$C(30)\% = 40 - 6.2 \ln(D) \quad \text{Eq. 1}$$

271 This fit both suggests the presence of crevasses below the lowermost crevasse trace imaged by our OPTV log  
272 (at a depth of 265 m) and is consistent with the difference between measured and modelled englacial  
273 temperatures at our field site (Figure 4c), suggesting that crevasses warmed englacial ice to a depth of at  
274 least  $\sim 400$  m. Fitting a logarithmic curve to this residual temperature ( $T_e$ ,  $^\circ\text{C}$ ) against depth, as illustrated in  
275 Figure 4c, yields a close match ( $R = 0.95$ ) described by:

$$T_e = 21.0 - 3.3 \ln(D) \quad \text{Eq. 2}$$

276 The similarity of the relationships between crevasse frequency and depth (Figure 4a; Eq. 1) and residual  
277 temperature and depth (Figure 4c; Eq. 2) lends support to our interpretation that crevasses propagate to at  
278 least 400 m below the surface of Store Glacier, warming ice to that depth by the presence and refreezing of  
279 crevasse-filling meltwater.

## 280 5 Summary and conclusions

281 Our OPTV log of a borehole drilled in a crevassed area of fast-moving Store Glacier, Greenland, has  
282 successfully imaging deep crevasses for the first time. Combining analysis of this log with thermo-mechanical  
283 modelling has revealed the following.

- 284 • Thirty-five traces of surface crevasses were imaged directly to a maximum depth of 265 m. It is possible  
285 that the borehole intersected crevasses below this, but that they could not be distinguished from the  
286 host ice. Approximately one third of these 35 traces were intersected below a depth of 100 m, and  
287 only 20% were intersected in the uppermost 40 m.
- 288 • The borehole intersected traces of crevasses that originally formed ~3 - 4 km upglacier. Despite drilling  
289 in an active crevasse field, and between two open crevasses spaced ~10 m apart, the borehole  
290 intersected no local crevasses. This indicates that the active local crevasses were shallow and/or did  
291 not deviate sufficiently from vertical to intersect the uppermost 325 m of the borehole.
- 292 • Of the 35 traces imaged, 28 showed evidence of having been filled with meltwater that subsequently  
293 refroze. This meltwater and its refreezing released heat, assumed to be responsible for warming the  
294 ice to a depth of ~400 m, suggesting crevasses extended to this depth - although not imaged below  
295 265 m by our OPTV log.
- 296 • Refreezing of crevasse-fill water commonly creates a distinctive ice layer formed of a planar bubble-  
297 free ice layer some cm to tens of cm thick that envelopes a planar mm-thick central layer of bubble-  
298 rich last-frozen ice.
- 299 • Once formed, crevasse traces represent a plane of weakness that may be reactivated during advection  
300 through the glacier. Visual analysis of layering in the borehole OPTV image suggests that reopening  
301 occurs preferentially along the bubble-rich last-frozen layer(s), which then refill and refreeze, creating  
302 additional new last-frozen layers.
- 303 • Reactivation of crevasses may occur annually with crevasses opening and filling in the late spring and  
304 early summer. Once filled, refreezing would occur when the flow of meltwater is no longer able to  
305 resist inward freezing from the crevasse walls. The time separating opening and closing is not known  
306 but is likely to be within the range of hours to months. Although our OPTV log indicates that the  
307 refrozen ice layers are individually some cm to tens of cm thick, it is not known whether crevasses  
308 opened and filled to greater widths than this, subsequently closing through a combination of  
309 mechanical closure and refreezing.
- 310 • The crevasse traces imaged by our OPTV log, supplemented by new ones formed downglacier, extend  
311 deep enough to survive ablation and reach the glacier terminus. Here, being planes of weakness, these  
312 traces likely precondition the precise location of rifting, iceberg fracture and calving.

## 313 Acknowledgments

314 This research was funded by the European Research Council as part of the RESPONDER project under the  
315 European Union's Horizon 2020 research and innovation program (Grant 683043). Hot water drilling and  
316 borehole logging equipment were also supported by an Aberystwyth University Capital Equipment Grant and  
317 NERC grants NE/J013544 and NE/K610026. TRC and RL were supported by a UK NERC Doctoral Training  
318 Partnership Studentship (Grant NE/L002507/1). We are grateful to Ann Andreasen and the Uummannaq  
319 Polar Institute for their kind hospitality, to Nicole Bienert and Sean Peters for assistance in the field, and to  
320 Katie Miles, Emma Docherty and Tom Chase for assistance in constructing sensor strings.

## 321 Data availability

322 The OPTV, temperature and modelling data presented herein are available from [https://figshare\\*...](https://figshare*...)

323

## 324 References

- 325 Boon, S., & Sharp, M. (2003). The role of hydrologically-driven ice fracture in drainage system evolution on  
326 an Arctic glacier. *Geophysical Research Letters*, *30*(18). doi:10.1029/2003gl018034
- 327 Bougamont, M., Christoffersen, P., Nias, I., Vaughan, D. G., Smith, A. M., & Brisbourne, A. (2019). Contrasting  
328 Hydrological Controls on Bed Properties During the Acceleration of Pine Island Glacier, West  
329 Antarctica. *Journal of Geophysical Research: Earth Surface*, *124*(1), 80-96. doi:10.1029/2018jf004707
- 330 Cardozo, N., & Allmendinger, R. W. (2013). Spherical projections with OSXStereonet. *Computers &  
331 Geosciences*, *51*, 193-205. doi:<https://doi.org/10.1016/j.cageo.2012.07.021>
- 332 Catania, G. A., Neumann, T. A., & Price, S. F. (2008). Characterizing englacial drainage in the ablation zone of  
333 the Greenland ice sheet. *Journal of Glaciology*, *54*(187), 567-578. doi:10.3189/002214308786570854
- 334 Chudley, T. R., Christoffersen, P., Doyle, S. H., Abellan, A., & Snooke, N. (2019). High-accuracy UAV  
335 photogrammetry of ice sheet dynamics with no ground control. *The Cryosphere*, *13*(3), 955-968.  
336 doi:10.5194/tc-13-955-2019
- 337 Chudley, T. R., Christoffersen, P., Doyle, S. H., Bougamont, M., Schoonman, C. M., Hubbard, B., & James, M.  
338 R. (2019). Supraglacial lake drainage at a fast-flowing Greenlandic outlet glacier. *Proceedings of the  
339 National Academy of Sciences*, 201913685. doi:10.1073/pnas.1913685116
- 340 Colgan, W., Steffen, K., McLamb, W. S., Abdalati, W., Rajaram, H., Motyka, R., . . . Anderson, R. (2011). An  
341 increase in crevasse extent, West Greenland: Hydrologic implications. *Geophysical Research Letters*,  
342 *38*(18). doi:10.1029/2011gl048491
- 343 Das, S. B., Joughin, I., Behn, M. D., Howat, I. M., King, M. A., Lizarralde, D., & Bhatia, M. P. (2008). Fracture  
344 Propagation to the Base of the Greenland Ice Sheet During Supraglacial Lake Drainage. *Science*,  
345 *320*(5877), 778-781. doi:10.1126/science.1153360
- 346 Doyle, S. H., Hubbard, A. L., Dow, C. F., Jones, G. A., Fitzpatrick, A., Gusmeroli, A., . . . Box, J. E. (2013). Ice  
347 tectonic deformation during the rapid in situ drainage of a supraglacial lake on the Greenland Ice  
348 Sheet. *The Cryosphere*, *7*(1), 129-140. doi:10.5194/tc-7-129-2013
- 349 Doyle, S. H., Hubbard, B., Christoffersen, P., Young, T. J., Hofstede, C., Bougamont, M., . . . Hubbard, A. (2018).  
350 Physical Conditions of Fast Glacier Flow: 1. Measurements From Boreholes Drilled to the Bed of Store  
351 Glacier, West Greenland. *Journal of Geophysical Research: Earth Surface*, *123*.  
352 doi:10.1002/2017JF004529
- 353 Gilbert, A., Sinisalo, A., Gurung, T. R., Fujita, K., Maharjan, S. B., Sherpa, T. C., & Fukuda, T. (2020). The  
354 influence of water percolation through crevasses on the thermal regime of a Himalayan mountain  
355 glacier. *The Cryosphere*, *14*(4), 1273-1288. doi:10.5194/tc-14-1273-2020
- 356 Goodsell, B., Hambrey, M. J., Glasser, N. F., Nienow, P., & Mair, D. (2005). The structural glaciology of a  
357 temperate valley glacier: Haut Glacier d'Arolla, Valais, Switzerland. *Arctic Antarctic and Alpine  
358 Research*, *37*(2), 218-232. Retrieved from <Go to ISI>://WOS:000229484200010
- 359 Hambrey, M. J. (1976). Structure of the glacier Charles Rabots Bre, Norway. *GSA Bulletin*, *87*(11), 1629-1637.  
360 doi:10.1130/0016-7606(1976)87<1629:Solgcr>2.0.Co;2
- 361 Hambrey, M. J., & Clarke, G. K. C. (2019). Structural Evolution During Cyclic Glacier Surges: 1. Structural  
362 Glaciology of Trapridge Glacier, Yukon, Canada. *Journal of Geophysical Research: Earth Surface*,  
363 *124*(2), 464-494. doi:10.1029/2018jf004869
- 364 Hambrey, M. J., & Lawson, W. (2000). Structural styles and deformation fields in glaciers: a review. *Geological  
365 Society, London, Special Publications*, *176*(1), 59-83. doi:10.1144/gsl.Sp.2000.176.01.06
- 366 Hambrey, M. J., & Müller, F. (1978). Structures and Ice Deformation in the White Glacier, Axel Heiberg Island,  
367 Northwest Territories, Canada. *Journal of Glaciology*, *20*(82), 41-66.  
368 doi:10.3189/S0022143000021213
- 369 Hofstede, C., Christoffersen, P., Hubbard, B., Doyle, S. H., Young, T. J., Diez, A., . . . Hubbard, A. (2018). Physical  
370 Conditions of Fast Glacier Flow: 2. Variable Extent of Anisotropic Ice and Soft Basal Sediment From  
371 Seismic Reflection Data Acquired on Store Glacier, West Greenland. *Journal of Geophysical Research:  
372 Earth Surface*, *123*. doi:10.1002/2017jf004297
- 373 Hubbard, B. (1991). Freezing-rate effects on the physical characteristics of basal ice formed by net adfreezing.  
374 *Journal of Glaciology*, *37*(127), 339-347. doi:10.3189/S0022143000005773
- 375 Hubbard, B., Cook, S., & Coulson, H. (2009). Basal ice facies: a review and unifying approach. *Quaternary  
376 Science Reviews*, *28*, 1956-1969. doi:10.1016/j.quascirev.2009.03.005

- 377 Hubbard, B., Luckman, A., Ashmore, D. W., Bevan, S., Kulesa, B., Kuipers Munneke, P., . . . Rutt, I. (2016).  
378 Massive subsurface ice formed by refreezing of ice-shelf melt ponds. *Nature Communications*, 7,  
379 11897. doi:10.1038/ncomms11897
- 380 Hubbard, B., Roberson, S., Samyn, D., & Merton-Lyn, D. (2008). Digital optical televueing of ice boreholes.  
381 *Journal of Glaciology*, 54(188), 823-830. doi:10.3189/002214308787779988
- 382 Hubbard, B., Tison, J.-L., Pattyn, F., Dierckx, M., Boereboom, T., & Samyn, D. (2012). Optical-televueer-based  
383 identification and characterization of material facies associated with an Antarctic ice-shelf rift. *Annals*  
384 *of Glaciology*, 53(60), 137-146.
- 385 Hubbard, B., Tison, J.-L., Philippe, M., Heene, B., Pattyn, F., Malone, T., & Freitag, J. (2013). Ice-shelf density  
386 reconstructed from optical-televueer borehole logging. *Geophysical Research Letters*,  
387 2013GL058023. doi:10.1002/2013gl058023
- 388 Humphrey, N., & Echelmeyer, K. (1990). Hot-water drilling and borehole closure in cold ice. *Journal of*  
389 *Glaciology*, 36(124), 287-298. Retrieved from <Go to ISI>://A1990EQ92000005
- 390 Joughin, I., Smith, B. E., Howat, I. M., Scambos, T., & Moon, T. (2010). Greenland flow variability from ice-  
391 sheet-wide velocity mapping. *Journal of Glaciology*, 56(197), 415-430.  
392 doi:10.3189/002214310792447734
- 393 Kamb, W. B. (1959). Ice petrofabric observations from Blue Glacier, Washington, in relation to theory and  
394 experiment. *Journal of Geophysical Research (1896-1977)*, 64(11), 1891-1909.  
395 doi:10.1029/JZ064i011p01891
- 396 Lovell, H., Fleming, E. J., Benn, D. I., Hubbard, B., Lukas, S., & Naegeli, K. (2015). Former dynamic behaviour  
397 of a cold-based valley glacier on Svalbard revealed by basal ice and structural glaciology  
398 investigations. *Journal of Glaciology*, 61(226), 309-328.
- 399 Lüthi, M. P., Ryser, C., Andrews, L. C., Catania, G. A., Funk, M., Hawley, R. L., . . . Neumann, T. A. (2015). Heat  
400 sources within the Greenland Ice Sheet: dissipation, temperate paleo-firn and cryo-hydrologic  
401 warming. *The Cryosphere*, 9(1), 245-253. doi:10.5194/tc-9-245-2015
- 402 Malone, T., Hubbard, B., Merton-Lyn, D., Worthington, P., & Zwiggelaar, R. (2013). Borehole and Ice Feature  
403 Annotation Tool (BIFAT): A program for the automatic and manual annotation of glacier borehole  
404 images. *Computers & Geosciences*, 51(0), 381-389.  
405 doi:<http://dx.doi.org/10.1016/j.cageo.2012.09.002>
- 406 Miles, K. E., Hubbard, B., Quincey, D. J., Miles, E. S., Sherpa, T. C., Rowan, A. V., & Doyle, S. H. (2018).  
407 Polythermal structure of a Himalayan debris-covered glacier revealed by borehole thermometry.  
408 *Scientific Reports*, 8(1). doi:10.1038/s41598-018-34327-5
- 409 Morlighem, M., Williams, C. N., Rignot, E., An, L., Arndt, J. E., Bamber, J. L., . . . Zinglensen, K. B. (2017).  
410 BedMachine v3: Complete Bed Topography and Ocean Bathymetry Mapping of Greenland From  
411 Multibeam Echo Sounding Combined With Mass Conservation. *Geophysical Research Letters*, 44(21),  
412 11,051-011,061. doi:10.1002/2017gl074954
- 413 Mottram, R. H., & Benn, D. I. (2009). Testing crevasse-depth models: a field study at Breiðamerkurjökull,  
414 Iceland. *Journal of Glaciology*, 55(192), 746-752. doi:10.3189/002214309789470905
- 415 Noël, B., van de Berg, W. J., van Wesseem, J. M., van Meijgaard, E., van As, D., Lenaerts, J. T. M., . . . van den  
416 Broeke, M. R. (2018). Modelling the climate and surface mass balance of polar ice sheets using  
417 RACMO2 – Part 1: Greenland (1958–2016). *The Cryosphere*, 12(3), 811-831. doi:10.5194/tc-12-811-  
418 2018
- 419 Nye, J. F. (1955). Comments on Dr. Loewe's Letter and Notes on Crevasses. *Journal of Glaciology*, 2(17), 512-  
420 514. doi:10.3189/S0022143000032652
- 421 Philippe, M., Tison, J.-L., Fjøsne, K., Hubbard, B., Kjær, H. A., Lenaerts, J. T. M., . . . Pattyn, F. (2016). Ice core  
422 evidence for a 20th century increase in surface mass balance in coastal Dronning Maud Land, East  
423 Antarctica. *The Cryosphere*, 10(5), 2501-2516. doi:10.5194/tc-10-2501-2016
- 424 Phillips, T., Rajaram, H., & Steffen, K. (2010). Cryo-hydrologic warming: A potential mechanism for rapid  
425 thermal response of ice sheets. *Geophysical Research Letters*, 37(20). doi:10.1029/2010gl044397
- 426 Pohjola, V. A. (1994). Tv-video observations of englacial voids in Storglaciären, Sweden. *Journal of Glaciology*,  
427 40(135), 231-240.
- 428 Poinar, K., Joughin, I., Lilien, D., Brucker, L., Kehrl, L., & Nowicki, S. (2017). Drainage of Southeast Greenland  
429 Firn Aquifer Water through Crevasses to the Bed. *Frontiers in Earth Science*, 5(5).  
430 doi:10.3389/feart.2017.00005

431 Price, S. F., Payne, A. J., Howat, I. M., & Smith, B. E. (2011). Committed sea-level rise for the next century  
432 from Greenland ice sheet dynamics during the past decade. *Proceedings of the National Academy of*  
433 *Sciences*. doi:10.1073/pnas.1017313108

434 Roberson, S., & Hubbard, B. (2010). Application of borehole optical televiewing to investigating the 3-D  
435 structure of glaciers: implications for the formation of longitudinal debris ridges, midre Lovenbreen,  
436 Svalbard. *Journal of Glaciology*, 56(195), 143-156. doi:10.3189/002214310791190802

437 Seguinot, J., Funk, M., Bauder, A., Wyder, T., Senn, C., & Sugiyama, S. (2020). Englacial Warming Indicates  
438 Deep Crevassing in Bowdoin Glacier, Greenland. *Frontiers in Earth Science*, 8(65).  
439 doi:10.3389/feart.2020.00065

440 van der Veen, C. J. (1998). Fracture mechanics approach to penetration of surface crevasses on glaciers. *Cold*  
441 *Regions Science and Technology*, 27(1), 31-47. doi:[https://doi.org/10.1016/S0165-232X\(97\)00022-0](https://doi.org/10.1016/S0165-232X(97)00022-0)

442 Weertman, J. (1973). Can a water-filled crevasse reach the bottom surface of a glacier? *IAHS Publ.*, 95, 139-  
443 145.

444